

# Reflectance of Antarctica from 3 to 5 $\mu\text{m}$ : discrimination of surface snow and cloud properties

WENDY M. CALVIN,<sup>1</sup> MARGARET MILMAN,<sup>2</sup> HUGH H. KIEFFER<sup>3</sup>

<sup>1</sup>*Department of Geological Sciences, University of Nevada, Reno, NV 89557, U.S.A.*

<sup>2</sup>*Department of Geology and Geophysics, University of Hawaii, Honolulu, HI 96822, U.S.A.*

<sup>3</sup>*Astrogeology Team, U.S. Geological Survey, 2255 North Gemini Drive, Flagstaff, AZ 86001, U.S.A.*

**ABSTRACT.** Current techniques of cloud discrimination in polar regions, ice surface temperature measurement, sea-ice and snowfield extent mapping often rely on data acquired in the region from 3 to 5  $\mu\text{m}$ . The Advanced Very High Resolution Radiometer (AVHRR) and the recently launched Moderate Resolution Imaging Spectroradiometer (MODIS) instrument on Terra have spectral bands in this region used for these purposes. Approaches often consider the radiance value in this spectral range in terms of a single equivalent brightness temperature. However, this spectral region contains contributions from both solar-reflected and thermal-emitted radiance, and a water ice reflectance peak at 3.7  $\mu\text{m}$  can be highly variable and a sensitive indicator of grain-size in icy particles either in clouds or as surface snow. In December 1992 the Galileo spacecraft, on its way to Jupiter, flew by and acquired images of Antarctica that included spectral coverage in 408 channels in the wavelength range 1–5  $\mu\text{m}$  with the Near Infrared Mapping Spectrometer (NIMS). The NIMS spectra provide a basis for the separation of the reflected and emitted components in this wavelength region. This separation then allows the examination of the observed variation of the reflected component with respect to cloud and surface ice properties. This analysis may help refine current algorithms for cloud discrimination in AVHRR and MODIS using channels from 3 to 5  $\mu\text{m}$ .

## INTRODUCTION

Multispectral datasets (commonly a few to ten channels in the visible and infrared), such as Landsat Thematic Mapper (TM) and Advanced Very High Resolution Radiometer (AVHRR), cover large areas on near-daily repeat cycles. This affords long-term monitoring capabilities, but ambiguity exists when separating clouds from snow and ice in polar or glacial scenes. The term “hyperspectral” has recently been coined to denote imaging datasets with hundreds of spectral channels such as the Airborne Visible/Infrared Imaging Spectrometer (AVIRIS).

Steffen and others (1993) have summarized the use of AVHRR data in polar regions for a variety of studies including cloud masking, ice surface temperature (IST), ice-concentration and lead monitoring, sea-ice motion and ice-sheet studies. Some of these applications rely on AVHRR band 3 which senses radiation in the wavelength range 3.55–3.93  $\mu\text{m}$ . In particular, this band has been found quite useful in identifying clouds, which is a prerequisite in studies of IST and mapping of ice type and extent (e.g. Massom and Comiso, 1994).

Kidder and Wu (1984) noted that clouds and snow cover, while similar in albedo in both visible and thermal AVHRR channels, had dramatically different albedos in band 3. Yamanouchi and Kawaguchi (1992) have modeled the emissivity variations in this band based on water droplets vs ice spheres, but thermal inversions, or the reflectance of a snow-covered surface seen through thin clouds, will introduce ambiguity. Current methods of cloud masking using

AVHRR typically rely on the apparent difference in brightness temperature between bands 3 and 4 (e.g. Yamanouchi and Kawaguchi, 1992; Sakellariou and others, 1993) or both the brightness difference and textural features seen in the visible and near-infrared bands (e.g. Key, 1990; Welch and others, 1992).

In development of algorithms for cloud discrimination in Moderate Resolution Imaging Spectroradiometer (MODIS) data, the channels from 3.5 to 4.0  $\mu\text{m}$  are also used (e.g. Ackerman and others, 1998). In particular, use of these channels for brightness-temperature differences was found to be the most accurate method of discriminating clouds over polar sea ice (Riggs and others, 1999). However, current methods often rely on a single equivalent brightness temperature ( $T_B$ ) for the MODIS channel centered on 3.82  $\mu\text{m}$ , and, as noted by Baum and others (2000), uncertainties are introduced by the contribution of both solar-reflected and thermally emitted fluxes at this wavelength.

In this paper we present hyperspectral data acquired in this spectral range and show that reflected and emitted contributions can be clearly separated. We then explore the variability of the purely reflected component and interpret this in terms of cloud and surface snow physical properties. Existing studies rely on the theoretical calculation of ice cloud particle size and scattering properties. The NIMS data provide unique observational constraints on these properties for a wavelength range where no previous hyperspectral observations exist. The methods developed may help refine algorithms for cloud and snow separation in both MODIS and AVHRR scenes.

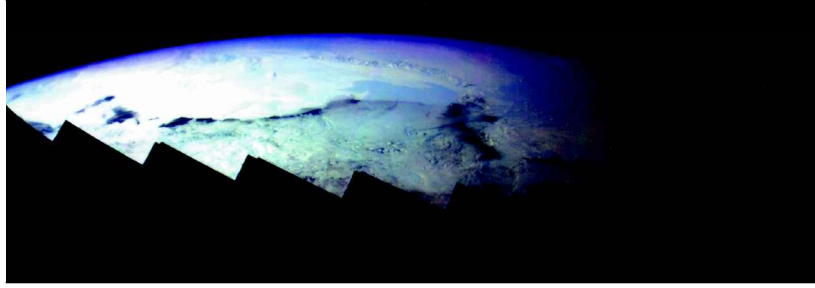


Fig. 2. SSI mosaic acquired at the same time as the NIMS spectral cube from Geissler and others (1995). Note the oblique geometry of the fly-by. Image shows cloud structures over the Ross Ice Shelf and the Transantarctic Mountains near the center.

**SPECTRAL REFLECTANCE OF SNOW AND ICE 1.0 TO 2.5  $\mu\text{m}$**

Techniques for the determination of snow physical properties from theoretical and laboratory spectral characteristics are well developed for the wavelength range less than 2.5  $\mu\text{m}$ .

Among the most commonly used theories for the calculation of snow albedo are those developed and summarized by Wiscombe and Warren (1980) and Warren (1982). Discrete-ordinate methods (Stamnes and others, 1988) are also used for calculating snow albedo because this allows for the determination of the reflected radiation at a particular bidirectional viewing geometry (e.g. Nolin and Dozier, 1993). Due to the asymmetric scattering of snow particles, significant variation in reflectance level can occur depending on incident and viewing geometries, particularly for large incidence angles and viewing geometries facing the sun.

High-spectral-resolution laboratory and field measurements of frost, snow and ice have also been widely performed at wavelengths less than 2.5  $\mu\text{m}$ . Laboratory measurements of the dependence of reflectance on grain-size and contaminant level have been made on laboratory-grown frosts by Clark (1981) and on natural snows by Sergent and others (1993). Field measurements of sea ice off the coast of Alaska were made by Grenfell and Perovich (1984), and a number of investigators have acquired data in polar regions, including Carlson and others (1993), Grenfell and others (1994) and De Abreu and others (1995). Both the theoretical and laboratory

measurements note the well-known spectral variation with grain-size, including decreased albedo at near-infrared wavelengths and saturation of absorption features at 1.5 and 2.0  $\mu\text{m}$ . Grenfell and others (1994) established the need for a two-layer approach in theoretical calculations which attempt to duplicate observed snow reflectance where fine grains overlay older, coarser grains, particularly at wavelengths greater than 1  $\mu\text{m}$ .

Based on the distinctive reflectance properties, remote-sensing studies have sought to derive and map snow grain-size. Nolin and Dozier (1993) simultaneously made field measurements during an AVIRIS overflight and developed a model to invert snow grain-size and water content using narrow spectral channels in the range 0.94–1.04  $\mu\text{m}$ . Bourdelles and Fily (1993) mapped grain-size in a cloud-free TM scene based on brightness levels, but determined different grain-sizes from the different bands. They found much smaller grains for the near-infrared wavelength bands, and larger grains for the 0.76–0.9  $\mu\text{m}$  band. They attributed these results to the presence of new snow overlying old snow, which is consistent with the models of Grenfell and others (1994).

**REFLECTANCE OF SNOW AND ICE FROM 3 TO 5  $\mu\text{m}$**

Although a large amount of work has been done on the spectral properties of ice at shorter wavelengths, only a few studies and observational constraints exist for the region from 3 to 5  $\mu\text{m}$ . In addition, while numerous studies compare theoretical calculations to direct observations of ice surfaces at shorter wavelengths, this comparison is missing from 3 to 5  $\mu\text{m}$ . Fine-grained surface snow and ice clouds have a strong reflectance peak near 3.7  $\mu\text{m}$ . This can be noted in reflectance data of frosts from Roush and others (1990) and in natural snows measured by Salisbury and others (1994). This peak is also clearly seen in the reflectance spectra of frosts from Fink and Larson (1975). This reflectance peak is a very sensitive indicator of grain-size in surface snow for grains less than a few hundred micrometers (Calvin and others, 1995), as seen in calculated and measured frost spectra in Figure 1. This grain-size effect permits the clear discrimination of snow, ice and water clouds in AVHRR band 3. That is, this peak will appear in fine-grained surface snow and in ice clouds but will be absent in old snow, wet snow and water clouds. For example, Hutchison and Locke (1997) have used AVHRR band 3 to discriminate snow from water clouds, but they do not account for snow grain-size effects or potential contributions from ice clouds. In the Antarctic, where surface temperatures are typically very low, this grain-size dependence can be used for ice cloud and surface frost discrimination.

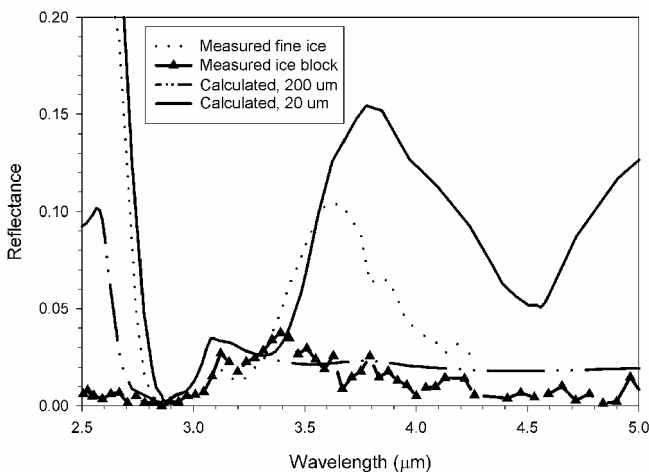


Fig. 1. Measured and calculated water ice at various grain-sizes. Measured frost and ice from Roush and others (1990). Calculations performed using the optical constants of Warren (1984) and the bidirectional radiative transfer model of Hapke (1981).

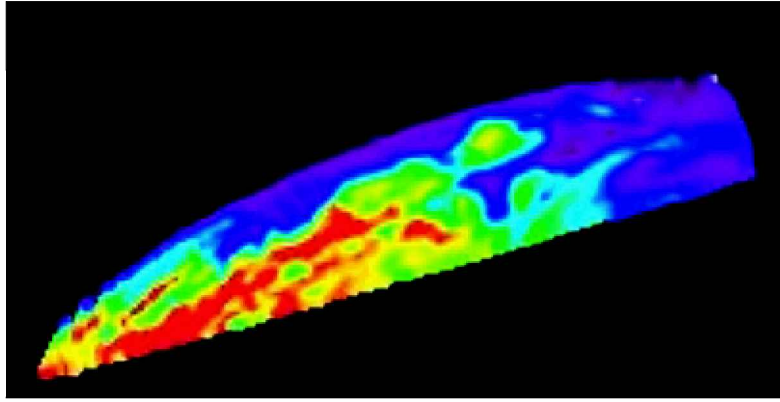


Fig. 3. Raw NIMS radiance in channel 282 at  $3.724 \mu\text{m}$ . Data values range from  $0.05$  (purple) to approximately  $0.55$  (red)  $\text{W m}^{-2} \text{sr}^{-1} \mu\text{m}^{-1}$ . Compare with Figure 2 for visible clouds and note that NIMS has poorer spatial resolution than the SSI camera.

Salisbury and others (1994) noted that the  $3.7 \mu\text{m}$  reflectance peak had a strong dependence on dry vs wet snow, but the peak was not obvious in many of their spectra of snow crusts, as these had grain-sizes larger than several hundred micrometers. One problem with this study was the lack of a cold chamber to preserve snow samples during measurement, so it is believed that grain aggregation and melting began almost immediately. Natural surfaces in Antarctica typically have surface grains which range from  $50$  to  $250 \mu\text{m}$  (Grenfell and others, 1994), and Brandt and Warren (1993) have shown that the infrared wavelengths will only be sensitive to the uppermost surface layer (a few tenths of millimeters in depth). The majority of cloud ice crystals range in particle size from  $10$  to  $100 \mu\text{m}$  (e.g. Francis, 1995). These values for both surface and cloud grain-sizes are well within the range where we expect a significant brightness variation of the  $3.7 \mu\text{m}$  peak. The particle-size values of clouds and surface snow are sufficiently different that these should be distinguishable based on the reflectance at this wavelength. Some ambiguity might be expected in regions of extremely fine surface snow, but the models of Grenfell and others (1994) suggest that even in Antarctica a large-grained component must be included to accurately model surface albedos.

## DESCRIPTION OF THE NIMS DATASET

A unique opportunity is afforded by observations made by a planetary spacecraft, Galileo, in a gravity-assist fly-by of the Earth where hyperspectral observations of Antarctica were made on 8 December 1992. The Near Infrared Mapping Spectrometer (NIMS) acquired images in 408 spectral channels from  $0.7$  to  $5.2 \mu\text{m}$  at a resolution of  $25 \text{ nm}$  full-width half-maximum for wavelengths longer than  $1 \mu\text{m}$  (Carlson and others, 1992). NIMS has 17 detectors, each of which samples a short, contiguous spectral range in successive grating steps. The instrument is essentially a “whisk-broom”-type scanner, mapping one spatial dimension through mirror motion and the other via spacecraft platform motion. Since only 17 wavelengths are acquired together, processing by the instrument team includes spatial binning of adjacent observations. In this way, spectra of the full 408 channels are built up over an effective area that is larger than the instrument’s instantaneous field of view. The resulting dataset is an image cube (two spatial dimensions and one spectral dimension) with an effective spatial

resolution of approximately  $20 \text{ km}$  per pixel. Figure 2 shows the concurrent Galileo Solid State Imager (SSI) mosaic in the red filter (Geissler and others, 1995). SSI and NIMS view the same area, but the SSI mosaic is slightly rotated to a

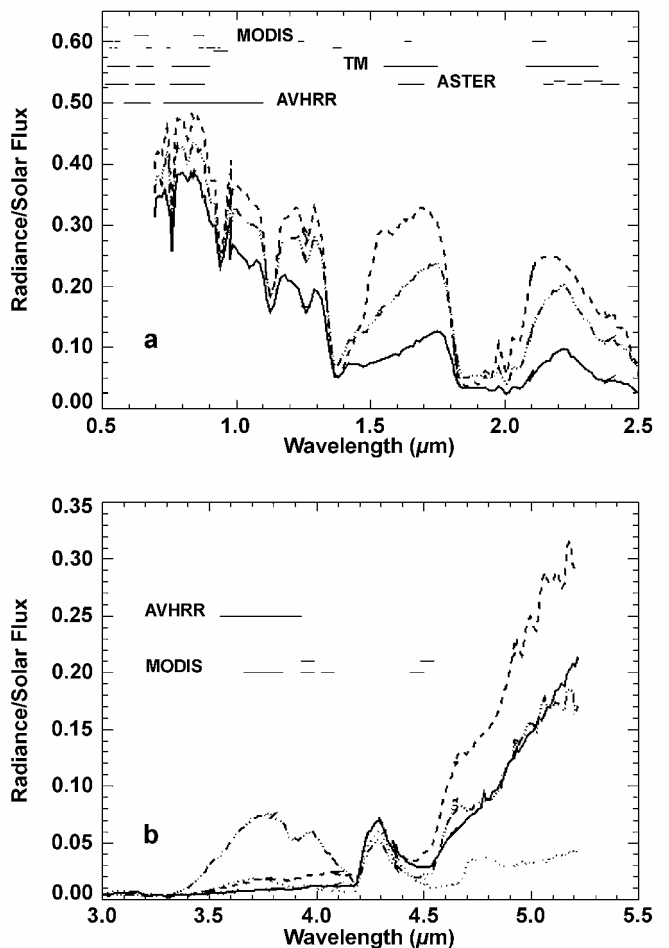


Fig. 4. Spectral variation within the NIMS data cube,  $0.7$ – $2.5 \mu\text{m}$  (a) and  $3$ – $5.5 \mu\text{m}$  (b). Spectra of individual pixels clearly show variations between normal atmospheric transmission (short dash in (a); solid in (b)) and increasing ice contributions as snow or ice cloud (dot-dash and solid in (a); dot-dash in (b)). Varying thermal emission is also evident in the strength of the radiance upturn beyond  $4 \mu\text{m}$  (b). Band-passes for AVHRR, ASTER and MODIS are plotted for comparison.

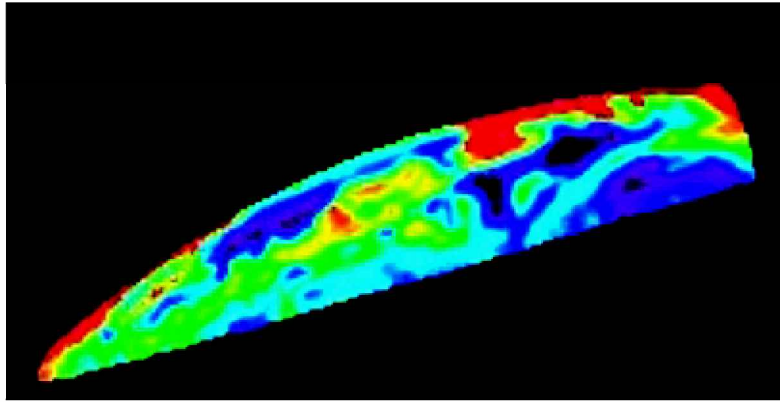


Fig. 6. The 3.7  $\mu\text{m}$  value corrected for thermal emission and viewing geometry. Compare with the raw image in Figure 3 and the derived temperatures in Figure 7.  $I/F$  values range from  $<0.1$  (black/purple) to  $>0.4$  (red). Green threshold is  $\sim 0.2$ , yellow is 0.3.

more horizontal position, and SSI has a much higher spatial resolution (1 km) than NIMS. The NIMS lower edge (straight line in Fig. 3) follows the bottom of the sawtooth of the SSI mosaic. Figure 2 also demonstrates the oblique view obtained during the Galileo fly-by.

Because the NIMS instrument was designed to function at the orbit of Jupiter where the solar flux is a factor of 25 lower than at Earth, many of the short-wavelength channels are saturated except in areas of high zenith angle. For a small strip over East Antarctica, however, pixels are unsaturated for the entire spectral range, thus allowing some comparison between ice grain-size determined using the 3.7  $\mu\text{m}$  ice reflectance peak and data at shorter wavelengths.

### CALIBRATION AND ANALYSIS OF THE NIMS DATA

Figures 3 and 4 clearly demonstrate the abundant spatial variability in brightness in the spectral range 3–5  $\mu\text{m}$ , which motivated our study to constrain the contribution from ice reflectance and from thermal emission. For the low tem-

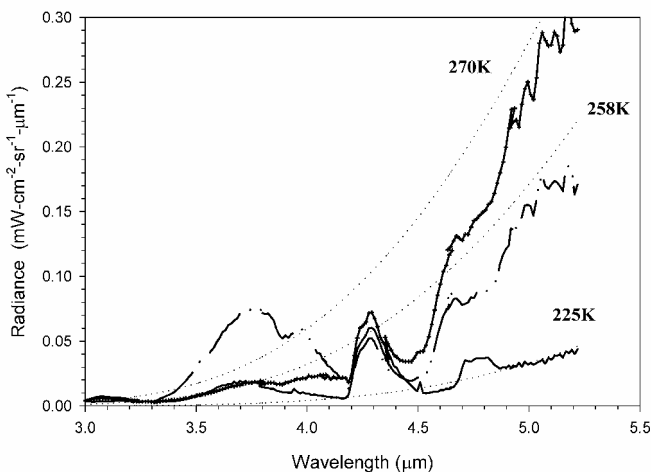


Fig. 5. Planck fits to the NIMS data. Note that the  $\text{CO}_2$  absorption from 4.2 to 4.4  $\mu\text{m}$  is inverted in all spectra, showing emission from warmer layers higher in the atmosphere. The atmospheric band from 4.7 to 4.9  $\mu\text{m}$  also inverts at the lowest temperatures. The selected spectra show how the intensity at 3.7  $\mu\text{m}$  depends both on ice peak strength and on thermal emission.

peratures over Antarctica, the intensity of the 3.7  $\mu\text{m}$  peak is related to first order to ice grain-size. As clouds typically have much smaller particles than surface snow, we can infer that the brightest regions in the NIMS “raw” 3.7  $\mu\text{m}$  radiance image are cloud-covered. This is corroborated through comparison of the NIMS image to the higher-resolution visible images acquired by the SSI instrument (Fig. 2). For medium bright pixels, however, thermal emission will contribute to the observed signal level at this wavelength.

Spectral diversity in the NIMS dataset is not limited to the 3.7  $\mu\text{m}$  peak value, as can be seen in selected spectra shown in Figure 4, where the radiance is corrected only for solar flux levels. Variability in the presence and grain-size of water ice can be noted by intensity variations near 1.6 and 2.2  $\mu\text{m}$ , and varying thermal emittance leads to changes in the spectral slope beyond 4.5  $\mu\text{m}$ . Within the NIMS data we therefore have the ability to independently assess thermal emission, so this contribution can be removed from the 3.7  $\mu\text{m}$  reflectance.

### Separation of thermal emission and reflectance

Raw NIMS radiance data at 3.7  $\mu\text{m}$  include variation introduced by ice grain-size effects, viewing angle and photometric effects and surface thermal emission. Analysis of the NIMS data cube first converted the instrument radiance value to a radiance factor ( $I/F$ ). The measured radiance ( $I$ ) is divided by the estimated flux ( $F$ ) with a simple geometric correction for viewing geometry and atmospheric transmission. The flux,  $F$ , is calculated as the sum of the solar reflectance,  $S$ , plus the best-fit Planck curve,  $P$ , which estimates the surface black-body emission ( $F = S + P$ ). The black-body component,  $P$ , was determined by the best-fit curve to the spectrum at wavelengths longer than 4  $\mu\text{m}$ , as shown in Figure 5. The photometric correction was calculated by dividing the  $I/F$  spectrum by the cosine of the incidence and emission angles ( $\cos i \cos e$ ). Each  $I/F$  spectrum in the image cube is then divided by a single MODTRAN-derived atmospheric transmission spectrum. This method only roughly removes gas-band absorptions; however, variable water is not expected to cause strong albedo variations in the 3.7  $\mu\text{m}$  ice peak. Variations in the contribution from  $\text{CO}_2$  gas-band absorption (often seen in emission over the cold Antarctic surface temperatures) will not be accurately corrected, as is seen in the final spectra. The resulting corrected values at 3.724  $\mu\text{m}$  are shown in Figure 6, and the derived temperatures in Figure 7.

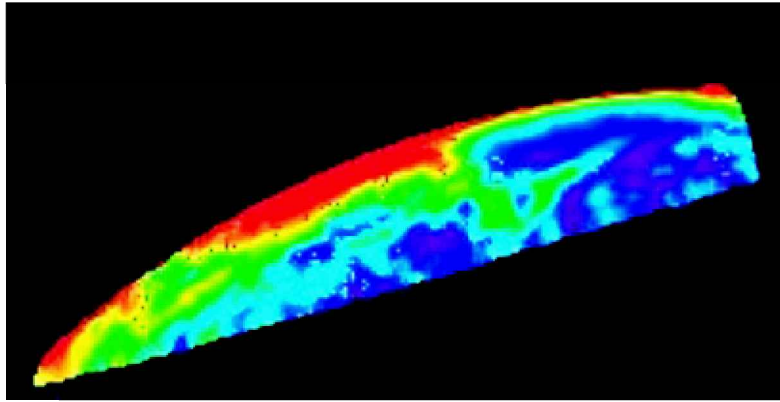


Fig. 7. Derived temperatures for the NIMS cube. Values range from  $< 240\text{ K}$  (purple/blue) to  $> 270\text{ K}$  (red). Maximum derived temperature was  $299\text{ K}$ ; minimum was  $237\text{ K}$ . Threshold for green is  $\sim 250\text{ K}$  and for yellow  $\sim 260\text{ K}$ .

## RESULTS AND DISCUSSION

Comparison of Figures 2 and 6 clearly shows that correction for the thermal-emission pedestal makes a dramatic difference to apparent ice grain-size as mapped at  $3.72\text{ }\mu\text{m}$ . While some large-scale features are similar, such as the boot-shaped blue area to the right, thermal-contribution removal highlights peak-strength subtleties in the center of the image (yellow to red in Fig. 6). This area corresponds to cloud structures over the Ross Ice Shelf (seen more clearly in the SSI image in Figure 2), a feature that is also seen in the concurrent AVHRR image acquired within 1 hour of the Galileo fly-by.

The  $I/F$  values range from  $< 0.1$  to  $\sim 0.6$  in Figure 6. Figure 8 shows that the thermal contribution has been reasonably well compensated (all spectra have similar  $I/F$  values longer than  $\sim 4.5\text{ }\mu\text{m}$ ) while dramatic variation in the  $3.7\text{ }\mu\text{m}$  ice peak strength remains. Where shorter-wavelength data are available, they suggest that the  $I/F$  correction over-

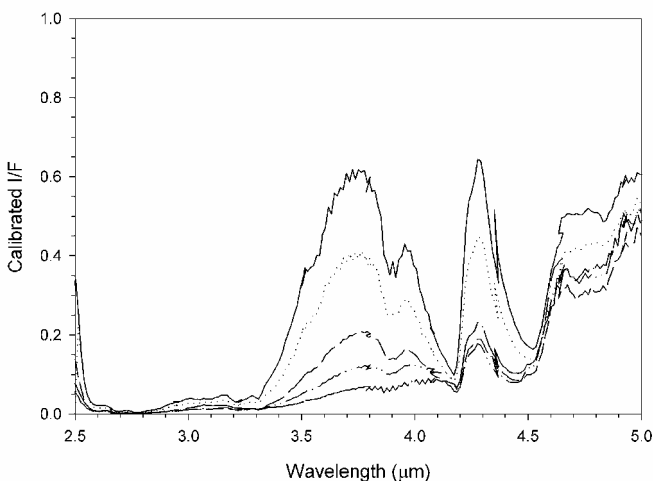


Fig. 8. Spectra corrected for viewing geometry and thermal emission. Note that the thermal contribution ( $> 4.5\text{ }\mu\text{m}$ ) has been mostly equalized, while substantial variation in the  $3.7\text{ }\mu\text{m}$  ice peak strength remains. Accurate correction for the  $\text{CO}_2$  gas absorption (inverted peak between  $4.2$  and  $4.5\text{ }\mu\text{m}$ ) was not attempted. Ice peak heights span the range of colors shown in Figure 6. Purple/black corresponds to the lowest peak in this figure, red the highest, with approximate color thresholds as indicated in Figure 6 caption.

estimates the true reflectance by a factor of 1.5 (i.e.  $I/F$  values greater than 1.0 occur at shorter wavelengths where the instrument was not saturated). This enhancement could be due to the simple approach to viewing geometry correction or the lack of consideration of the bidirectional reflectance distribution function of ice. Where available, however, short-wavelength data confirm the ice grain-size trends observed at  $3.72\text{ }\mu\text{m}$ . That is, a higher peak strength is consistent with finer ice (cloud ice-particle) size. Considering these factors, regions in Figure 6 that are aqua/green colored and warmer (yellow to red) are dominated by ice clouds whose particle sizes are less than  $20$  to  $50\text{ }\mu\text{m}$ . The only areas where surface snow dominates the image are in the black to purple colors in Figure 6. This also corresponds well with areas that appear clear in the SSI image (Fig. 2) and AVHRR data. We had hoped that surface grain-size variations could be determined with this approach, but the combination of the poor spatial resolution and oblique viewing geometry of NIMS limits the value of this dataset for that application.

The temperatures derived for the scene range from  $237$  to  $299\text{ K}$ , with generally warmer temperatures toward the limb and left of the image indicating sensitivity to solar direction (Fig. 7 and comparison to visual albedo in Fig. 2) and cooler temperatures over exposed surface regions to the right (blue areas in Fig. 6). The derived temperatures suggest that approaches which use a single equivalent brightness temperature for AVHRR band 3 to derive clouds may ambiguously confuse warmer regions with ice clouds. In particular, warm regions (green to red) to the left of the image (Fig. 7) are mapped in the thermal-removed ice grain-size image as likely surface areas (purple to blue) in Figure 6. Compare this also to the raw radiance values (green to red colors) in Figure 3, which would suggest this region might be cloud-covered.

## FUTURE DIRECTIONS

The addition of this hyperspectral dataset provides a new framework for cloud discrimination using channels near  $3.8\text{ }\mu\text{m}$  in AVHRR and MODIS data. There are five AVHRR scenes acquired on the same day of the Galileo fly-by. Future work will explore the traditional cloud-masking techniques applied to AVHRR data and will compare these with a method that, similar to the NIMS analysis, first separates reflected and emitted contributions at this wavelength. Difficulties could arise due to the poor signal-to-

noise ratio in this AVHRR band, and extrapolation of this technique to MODIS data will also be explored.

## ACKNOWLEDGEMENTS

We would like to thank the NIMS Principal Investigator, R. Carlson, for access and help with the NIMS data analysis, and P. Geissler for providing the SSI mosaic. This work was supported by the NASA Remote Sensing in Glaciology program to W. Calvin, initially at the U.S. Geological Survey and subsequently at the University of Nevada, Reno. M. Milman participated via the U.S. National Science Foundation (NSF) Research Experience for Undergraduates (REU) program offered through Northern Arizona University's Physics and Astronomy Department. H. Kieffer's participation was supported by both the Advanced Spaceborne Thermal Emission and Reflection Radiometer (ASTER) and NIMS instrument teams. We greatly appreciate the constructive criticism from J. Key and the anonymous reviewers of the manuscript. W.M.C. would like to thank A.K. for the encouragement.

## REFERENCES

Ackerman, S. A., K. I. Strabala, P. W. P. Menzel, R. A. Frey, C. C. Moeller and L. E. Gumley. 1998. Discriminating clear sky from clouds with MODIS. *J. Geophys. Res.*, **103**(D24), 32,141–32,157.

Baum, B. A. and 6 others. 2000. Remote sensing of cloud properties using MODIS airborne simulator imagery during SUCCESS. 1. Data and models. *J. Geophys. Res.*, **105**(D9), 11,767–11,780.

Bourdelle, B. and M. Fily. 1993. Snow grain-size determination from Landsat imagery over Terre Adélie, Antarctica. *Ann. Glaciol.*, **17**, 86–92.

Brandt, R. E. and S. G. Warren. 1993. Solar-heating rates and temperature profiles in Antarctic snow and ice. *J. Glaciol.*, **39**(131), 99–110.

Calvin, W. M., R. N. Clark, R. H. Brown and J. R. Spencer. 1995. Spectra of the icy Galilean satellites from 0.2 to 5  $\mu\text{m}$ : a compilation, new observations, and a recent summary. *J. Geophys. Res.*, **100**(E9), 19,041–19,048.

Carlson, R. W., P. R. Weissman, W. D. Smythe, J. C. Mahoney and the NIMS science and engineering team. 1992. Near-infrared mapping spectrometer experiment on Galileo. *Space Science Reviews*, **60**(1–4), 457–502.

Carlson, R. W., T. Arakelian and W. D. Smythe. 1993. Spectral reflectance of Antarctic snow: "ground truth" and spacecraft measurements. *Antarct. J. U.S.*, **27**(5), 296–298.

Clark, R. N. 1981. The spectral reflectance of water–mineral mixtures at low temperatures. *J. Geophys. Res.*, **86**(B4), 3074–3086.

De Abreu, R. A., D. G. Barber, K. Misurak and E. F. LeDrew. 1995. Spectral albedo of snow-covered first-year and multi-year sea ice during spring melt. *Ann. Glaciol.*, **21**, 337–342.

Fink, U. and H. P. Larson. 1975. Temperature dependence of the water–ice spectrum between 1 and 4 microns: application to Europa, Ganymede and Saturn's rings. *Icarus*, **24**(4), 411–420.

Francis, P. N. 1995. Some aircraft observations of the scattering properties of ice crystals. *J. Atmos. Sci.*, **52**(8), 1142–1154.

Geissler, P., W. R. Thompson, R. Greenberg, J. Moerseh, A. McEwen and C. Sagan. 1995. Galileo multispectral imaging of the Earth. *J. Geophys. Res.*, **100**(E8), 16,895–16,906.

Grenfell, T. C. and D. K. Perovich. 1984. Spectral albedos of sea ice and incident solar irradiance in the southern Beaufort Sea. *J. Geophys. Res.*, **89**(C3), 3573–3580.

Grenfell, T. C., S. G. Warren and P. C. Mullen. 1994. Reflection of solar radiation by the Antarctic snow surface at ultraviolet, visible, and near-infrared wavelengths. *J. Geophys. Res.*, **99**(D9), 18,669–18,684.

Hapke, B. 1981. Bidirectional reflectance spectroscopy. 1. Theory. *J. Geophys. Res.*, **86**(B4), 3039–3054.

Hutchison, K. D. and J. K. Locke. 1997. Snow cover identification through cirrus-cloudy atmospheres using daytime AVHRR imagery. *Geophys. Res. Lett.*, **24**(14), 1791–1794.

Key, J. 1990. Cloud cover analysis with Arctic advanced very high resolution radiometer data. 2. Classification with spectral and textural measures. *J. Geophys. Res.*, **95**(D6), 7661–7675.

Kidder, S. Q. and H.-T. Wu. 1984. Dramatic contrast between low clouds and snow cover in daytime 3.7  $\mu\text{m}$  images. *Mon. Weather Rev.*, **112**(11), 2345–2346.

Massom, R. and J. C. Comiso. 1994. The classification of Arctic sea ice types and the determination of surface temperature using advanced very high resolution radiometer data. *J. Geophys. Res.*, **99**(C3), 5201–5218.

Nolin, A. W. and J. Dozier. 1993. Estimating snow grain size using AVIRIS data. *Remote Sensing Environ.*, **44**(2–3), 231–238.

Riggs, G. A., D. K. Hall and S. A. Ackerman. 1999. Sea ice extent and classification mapping with the Moderate Resolution Imaging Spectrometer Airborne Simulator (MAS). *Remote Sensing Environ.*, **68**(2), 152–163.

Roush, T. L., J. B. Pollack, F. C. Witteborn, J. D. Bregman and J. P. Simpson. 1990. Ice and minerals on Callisto: a reassessment of the reflectance spectra. *Icarus*, **86**(2), 355–382.

Sakellariou, N. K., H. G. Leighton and Z. Li. 1993. Identification of clear and cloudy pixels at high latitudes from AVHRR radiances. *Int. J. Remote Sensing*, **14**(10), 2005–2024.

Salisbury, J. W., D. M. D'Aría and A. Wald. 1994. Measurements of thermal infrared spectral reflectance of frost, snow, and ice. *J. Geophys. Res.*, **99**(B12), 24,235–24,240.

Sergent, C., E. Pougatch, M. Sudul and B. Bourdelle. 1993. Experimental investigation of optical snow properties. *Ann. Glaciol.*, **17**, 281–287.

Stamnes, K., S.-C. Tsay, W. Wiscombe and K. Jayaweera. 1988. Numerically stable algorithm for discrete-ordinate-method radiative transfer in multiple scattering and emitting layered media. *Appl. Opt.*, **27**(12), 2502–2509.

Steffen, K. and 11 others. 1993. Snow and ice applications of AVHRR in polar regions: report of a workshop held in Boulder, Colorado, 20 May 1992. *Ann. Glaciol.*, **17**, 1–16.

Warren, S. G. 1982. Optical properties of snow. *Rev. Geophys. Space Phys.*, **20**(1), 67–89.

Warren, S. G. 1984. Optical constants of ice from the ultraviolet to the microwave. *Appl. Opt.*, **23**(8), 1206–1225.

Welch, R. M., S. K. Sengupta, A. K. Goroch, P. Rabindra, N. Rangaraj and M. S. Navar. 1992. Polar cloud and surface classification using AVHRR imagery: an intercomparison of methods. *J. Appl. Meteorol.*, **31**(5), 405–420.

Wiscombe, W. J. and S. G. Warren. 1980. A model for the spectral albedo of snow. I. Pure snow. *J. Atmos. Sci.*, **37**(12), 2712–2733.

Yamanouchi, T. and S. Kawaguchi. 1992. Cloudy distribution in the Antarctic from AVHRR data and radiation measurements at the surface. *Int. J. Remote Sensing*, **13**(1), 111–127.